

6H-SiC microdisk torsional resonators in a “smart-cut” technology

Rui Yang,¹ Zenghui Wang,¹ Jaesung Lee,¹ Kalyan Ladhane,² Darrin J. Young,² and Philip X.-L. Feng^{1,a)}

¹Department of Electrical Engineering and Computer Science, Case School of Engineering Case Western Reserve University, 10900 Euclid Avenue, Cleveland, Ohio 44106, USA

²Department of Electrical and Computer Engineering, University of Utah, Salt Lake City, Utah 84112, USA

(Received 8 December 2013; accepted 23 February 2014; published online 6 March 2014)

We report on experimental demonstration of high frequency torsional resonators based on microdisk structures enabled by a “smart-cut” 6H-silicon carbide (6H-SiC) technology. Circular microdisks axially supported by pairs of thin tethers, with diameters of $\sim 5\text{--}15\ \mu\text{m}$, exhibit torsional-mode micromechanical resonances with frequency of $\sim 1\text{--}60\ \text{MHz}$, and quality (Q) factors up to 1280 at room temperature in moderate vacuum ($\sim 10\ \text{mTorr}$). Measured intrinsic thermomechanical vibrations of a microdisk with diameter $d \approx 15.9\ \mu\text{m}$ (and triangular cross-section tethers with width $w_T \approx 1.5\ \mu\text{m}$, length $L_T \approx 2\ \mu\text{m}$, and thickness $t_T \approx 0.4\ \mu\text{m}$) demonstrate a torque resolution of $S_T^{1/2} \approx 3.7 \times 10^{-20}\ (\text{N m})/\sqrt{\text{Hz}}$, a force sensitivity of $S_F^{1/2} \approx 5.7\ \text{fN}/\sqrt{\text{Hz}}$, and an angular displacement sensitivity of $S_\theta^{1/2} \approx 4.0 \times 10^{-8}\ \text{rad}/\sqrt{\text{Hz}}$. By examining devices with varying disk size, different tether shape, width, and length, and by combining experimental data and theoretical calculations, we depict the scaling pathways for ultrasensitive torsional resonant sensors based on this smart-cut 6H-SiC platform. © 2014 AIP Publishing LLC.

[<http://dx.doi.org/10.1063/1.4867866>]

Continuing miniaturization of mechanical sensors and actuators into micro- and nano-electromechanical systems (MEMS and NEMS) has helped revolutionize integrated positioning, timing, communication, sensing, and other functions in today’s pervasive mobile devices. In fundamental studies, vibrating NEMS resonators have enabled ultrasensitive detections of a wide spectrum of physical quantities (e.g., charge, force, displacement, and surface adsorbed mass) with unprecedented sensitivities.^{1–7} Realizing such functions generally relies on exploiting certain vibrational modes in the MEMS/NEMS, including flexural, bulk acoustic, and torsional vibrations.^{8,9} Among these, torsional modes allow for direct coupling forces, torques and other external stimuli into rotations, thus offering a unique platform with versatile sensing modalities. With advancements in micro/nanofabrication techniques, miniaturized torsional-mode devices benefit from smaller torsional spring constants by shrinking the rotating tethers (springs), as well as the widely employed torsional paddles that provide adequate axial lengths for torques or sizable capturing areas, to be highly responsive to various stimuli. A number of torsional resonators based on MEMS and NEMS structures^{1,10–21} have been explored over the last two decades, demonstrating potential for electrometer,¹ thermal sensing,¹⁵ magnetometry,^{16,17} optomechanics,¹⁸ surface adsorbate mass sensing,¹⁹ atomic force microscopy,²⁰ and torque-modulated bandgap oscillations.²¹ The structural materials for these torsional devices have mainly been limited to Si and SiN layers with well-established lithographical and surface micro/nanomachining processes, or chemically synthesized nanostructures demanding careful assembly (e.g., carbon nanotubes²¹). It is desirable to explore these torsional devices and functions in new materials; particularly it is

intriguing to create torsional resonators based on advanced materials that are complementary to Si, and that can withstand hostile environments such as in high temperature, chemically aggressive (reactive or corrosive) gases, high wear, or radiative systems. Such durability will help to lend the high sensitivities of torsional resonators to demanding and critical applications, including reading out and long-term monitoring of temperature, force, and other physical quantities in combustion and radiation environments.

Silicon carbide (SiC),²² with a combination of outstanding electrical, mechanical, thermal properties, and chemical inertness and durability,²³ has been a technologically important material that is especially established for high-temperature, harsh-environment electronics,²⁴ and transducers,²⁵ including MEMS/NEMS. Among many types of SiC crystals, single-crystal 6H-SiC has been attractive as a desirable structural material for MEMS/NEMS, with advantageous attributes such as high Young’s modulus ($E_Y \sim 450\ \text{GPa}$ or higher), very high thermal conductivity ($490\ \text{W}/(\text{m K})$), wide bandgap ($3.0\ \text{eV}$), and availability in high-quality wafers. The progress, however, has been quite limited, largely due to the difficulties in device fabrication. While thin films (sometimes multilayers) and surface micro/nanomachining are often required for making MEMS/NEMS resonators, high-quality 6H-SiC predominately comes in bulk single crystal instead of thin films. Depositing 6H-SiC thin films has been explored, with results showing a mixture of 6H- and 3C-SiC polycrystalline layer on Si;²⁶ the desired hetero-epitaxial growth of single-crystal 6H-SiC films on sacrificial layers (e.g., Si and SiO₂), however, remains challenging. Bulk nano/micromachining of single-crystal 6H-SiC has been attempted to fabricate suspended nanobeams²⁷ and microcantilevers,²⁸ by using high-power reactive ion etching (RIE) techniques such as electron cyclotron resonance (ECR)²⁷ and inductively coupled plasmas (ICP).²⁸ But such processes of sculpturing micro/nanostructures out of *bulk*

^{a)}Author to whom correspondence should be addressed. Electronic mail: philip.feng@case.edu.

6H-SiC wafers (instead of thin films) are not only very time consuming but also require deposited metal masks and still lack precision when thin films and small dimensions are required for devices.

In this work, we explore a “smart-cut” 6H-SiC technology that produces thin layers of single crystal 6H-SiC on top of oxidized silicon wafers; and in this platform, we demonstrate 6H-SiC torsional resonators based on circular microdisks supported by pairs of thin tethers. We measure both the undriven thermomechanical vibrations and the optically driven resonances of these devices. By varying disk diameter and tether shape, we investigate the scaling of device performance. Combining measurements and analysis, we delineate the roadmaps of resonant sensitivities for these 6H-SiC torsional resonators.

The devices take the form of a circular microdisk suspended between two thin tethers, and exhibit torsional motions around the diameter through the tethers (Figs. 1(a)–1(c)). We first make a single-crystal 6H-SiC thin layer on top of a SiO₂-on-Si wafer by using a “smart-cut” process, as illustrated in Figs. 1(d)–1(g). The fabrication starts with a commercially available 6H-SiC wafer with a thickness around 250 μm. Energized protons (200 keV) are implanted with a peak concentration of ~1.2 μm below the surface, creating micro-cavities in the SiC lattice.²⁹ After being treated by oxygen plasma to activate the surfaces, the H⁺-implanted SiC wafer and a Si wafer with ~0.5 μm SiO₂ on top are brought together to perform wafer bonding. At 1000 °C, the splitting of SiC is initiated by the micro-cavities in the lattice where proton concentration is the highest, resulting in a bonded SiC-SiO₂-Si wafer. The wafer is further annealed at 1150 °C, to reduce defect density and enhance bonding strength.

We pattern circular microdisks on the top SiC film with focused ion beam (FIB, 30 kV Ga⁺ ion, beam current 1 to 7 nA), by raster scanning the FIB in pre-designed patterns and milling SiC in the selected regions. This “lithography-free” high-resolution FIB method obviates challenging etching processes for SiC and allows for rapid prototyping of device structures in various geometries, with

high efficiency and throughput (e.g., FEI NanoBuilder™). We systematically vary disk diameters and tether shapes and dimensions to investigate the scaling effects on devices resonance performance. We then release the resonator structure using buffered oxide etch (BOE) (Figs. 1(h) and 1(i)). The resulting uniform air gap (replacing the initial SiO₂ sacrificial layer) between the SiC device and underneath Si surface facilitates highly sensitive spatial-resolved interferometric motion detection by providing an even background.

We measure the 6H-SiC microdisk resonators with sensitive laser interferometry techniques,³⁰ by using a 632.8 nm He-Ne laser with an on-device spot size of ~1 μm and a laser power of 10 mW. We employ an X-Y stage to laterally scan the laser spot across the device area and spatially map the torsional resonance mode shape (Fig. 2(a)). We conduct the experiment using a 632.8 nm laser due to the wide bandgap (3.0 eV) of 6H-SiC, which results in minimal optical absorption at this wavelength. This enables the usage of sufficiently high laser power, which produces exceptional signal-to-noise ratio without undesired heating effect. All measurements are performed in vacuum (~10 mTorr) and at room temperature. With the highly sensitive optical interferometry, we are able to measure the un-driven thermomechanical motions in these SiC resonators. At room temperature, the unceasing Brownian motions of the devices are exemplified in the frequency domain as thermomechanical resonance modes as described by the fluctuation-dissipation theorem. The thermomechanical noise is recorded with a spectrum analyzer. The measured noise spectrum for a $d \approx 10 \mu\text{m}$ device with tethers of rectangular cross section is shown in Fig. 2(b). We fit the measured total voltage-domain spectral density, $S_{v,\text{total}}^{1/2}$, to the model of a damped simple harmonic resonator

$$S_{v,\text{total}}^{1/2}(\omega) = \sqrt{\Re^2\left(\frac{4\omega_0 k_B T}{QM_{\text{eff}}(\omega_0^2 - \omega^2)^2 + (\omega_0 \omega / Q)^2}\right) + S_{v,\text{sys}}}, \quad (1)$$

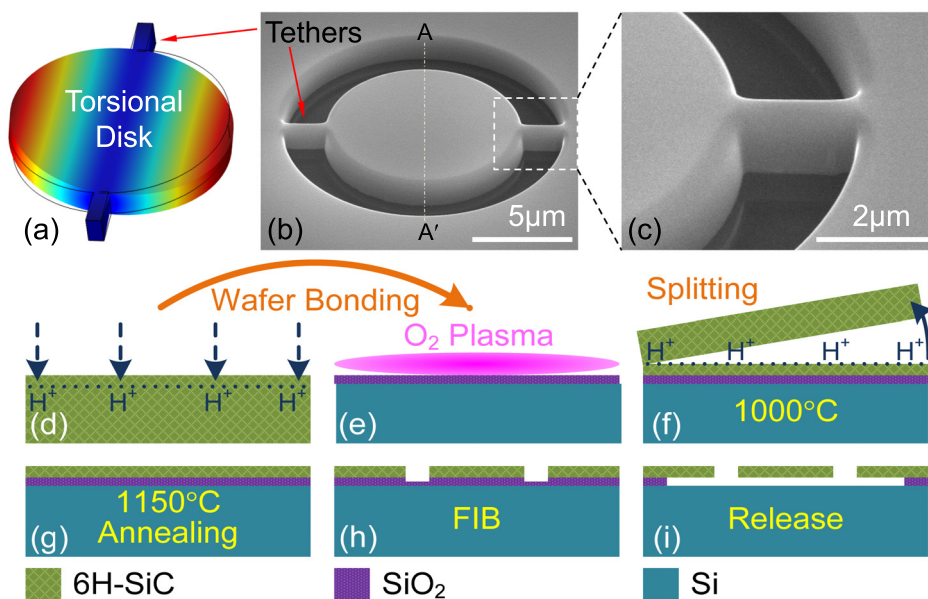


FIG. 1. Device concept and fabrication process of 6H-SiC torsional resonators based on tether-supported circular microdisks. (a) Illustration of the designed torsional mode shape by finite element modeling (FEM, in COMSOL). (b) A scanning electron micrograph (SEM) image of a suspended torsional microdisk. (c) A zoom-in view of the tether area in (b). (d)–(i) Fabrication process for making the torsional microdisks using the “smart-cut” technology, showing (d) proton (H⁺) implantation into single-crystal 6H-SiC wafer, (e) wafer bonding of 6H-SiC onto oxidized Si substrate, (f) splitting of 6H-SiC leaving a thin 6H-SiC layer on SiO₂, (g) annealing, (h) FIB patterning and nanomachining, (i) release of the resonators by BOE of the sacrificial SiO₂ layer. (h) and (i) are cross-sectional views indicated by the dashed line AA' in (b).

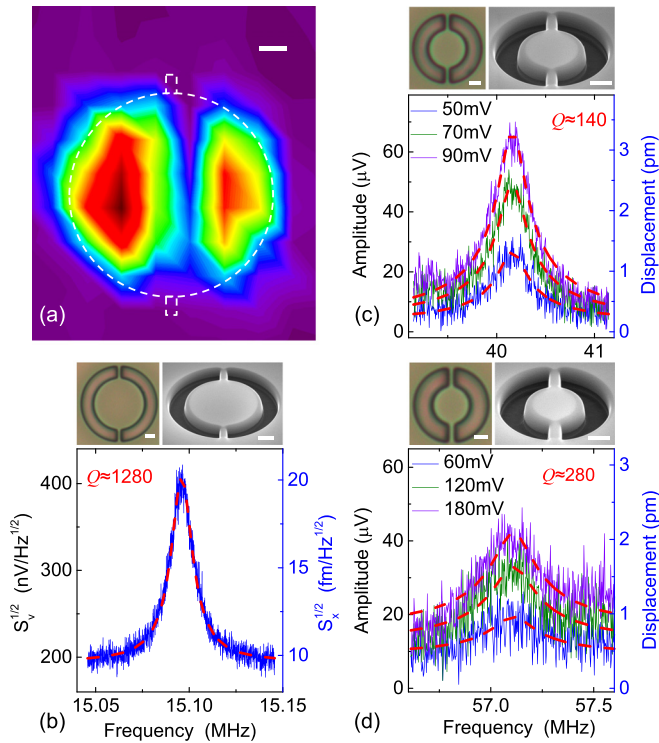


FIG. 2. Measured torsional resonance characteristics from microdisks with shrinking diameters. (a) Spatial mapping of the torsional mode shape of a device with disk diameter $d \approx 15.9 \mu\text{m}$ and tethers of triangular cross section (tether width $w_T \approx 1.5 \mu\text{m}$, thickness $t_T \approx 0.4 \mu\text{m}$, length $L_T \approx 2 \mu\text{m}$). (b) Undriven, thermomechanical resonance of a torsional microdisk with $d \approx 10 \mu\text{m}$ and tethers of rectangular cross section ($w_T \approx 0.7 \mu\text{m}$, $t_T \approx 1.2 \mu\text{m}$, $L_T \approx 2 \mu\text{m}$). Left axis shows the voltage domain noise spectral density, while the right axis translates the signal to the displacement domain. (c) and (d) Measured driven resonances of $d \approx 6 \mu\text{m}$ and $d \approx 5 \mu\text{m}$ microdisks, respectively, with the same rectangular tether as in (b). Blue, olive, and purple curves denote measured responses at different excitations (legends). Left axis shows the voltage-domain signal amplitude, while the right axis is the corresponding displacement-domain signal. All panels: red dashed lines show fittings to the measured resonances, with optical and SEM images from the respective devices shown above the data. All scale bars: $2 \mu\text{m}$.

where ω_0 , Q , and M_{eff} are the angular resonance frequency, quality factor, and effective mass of the resonance, k_B is the Boltzmann constant, T is the temperature, $S_{v,\text{sys}}$ is the system background, and \mathfrak{R} is the responsivity defined by \mathfrak{R}

$= S_v^{1/2}/S_x^{1/2}$ (where $S_v^{1/2}$ and $S_x^{1/2}$ are the noise spectral density in the voltage and displacement domain, respectively). From fitting, we extract the quality factor $Q \approx 1280$, leading to an $f \times Q$ product of $1.9 \times 10^{10} \text{ Hz}$ for this device.

Beyond the un-driven intrinsic Brownian motions, we also measure the driven response by optically exciting the resonances. To drive the device motion, a modulated 405 nm blue diode laser is focused near the device. With its photon energy (3.07 eV) above the bandgap of 6H-SiC, the intensity-modulated 405 nm laser effectively induces periodic heating and thus thermal expansion and periodic motions in the device. A radio-frequency (RF) network analyzer is employed for both modulating the laser intensity and measuring the responses of the driven resonances. Figures 2(c) and 2(d) show the measurements from devices with $d \approx 6 \mu\text{m}$ and $d \approx 5 \mu\text{m}$ under different driving amplitudes, respectively.

We further investigate resonance scaling of these devices. We fabricate devices with varying diameters and different tether shapes (rectangular *versus* triangular cross sections) (Figs. 3(a) and 3(b)), and perform theoretical calculations as well as finite element modeling (FEM, with COMSOLTM simulations). The resonance frequency of a torsional resonator can be calculated using $f_0 = (1/2\pi)\sqrt{k_T/I}$, where $k_T = J_T E_Y / [L_T(\nu + 1)]$ is the torsional spring constant and, J_T is the torsional area moment of inertia, and I is the mass moment of inertia, all of which depend on the exact shape and size (with ν being Poisson ratio).^{31,32} In Fig. 3(c), we show the resonance frequency *versus* device diameter, plotting theoretical calculation, FEM simulation, and experimental results, all of which show good agreements between each other. The resonance frequency clearly increases with decreasing disk diameter, as expected. We also plot the measured Q in the same figure. With similar tether dimensions, larger disks offer higher Q s, implying a correlation to the diameter-to-tether width (d/w_T) ratio, and suggesting clamping loss in these devices.³³

The fundamental limits of the device performance, such as force and displacement sensitivities, are set by the thermal fluctuations in these devices. We first estimate the on-resonance thermomechanical displacement noise of these devices using $S_{x,\text{th}}^{1/2} = \sqrt{4k_B T Q / (\omega_0^3 M_{\text{eff}})}$. In Fig. 3(d),

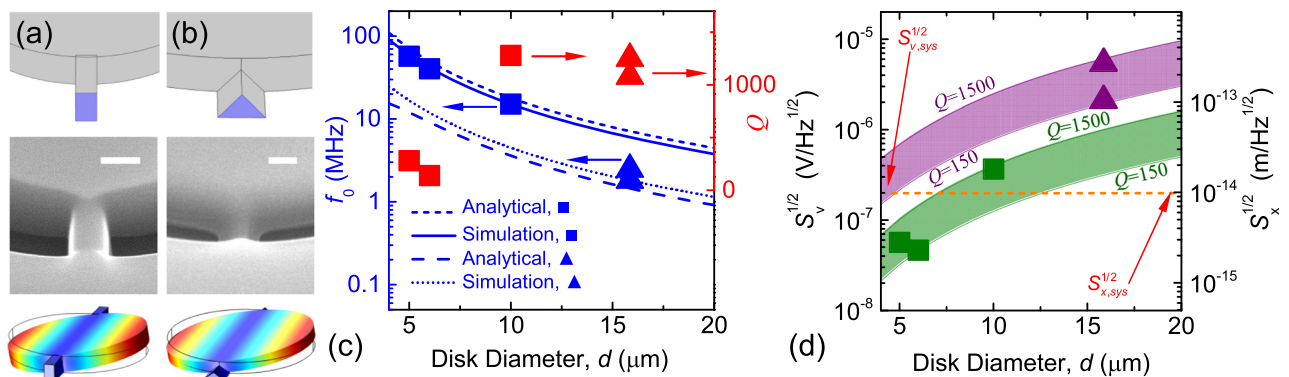


FIG. 3. Scaling of frequency, quality (Q) factor, and thermomechanical resonance with diameter of circular microdisk. (a) and (b) Illustrative comparison between tethers with rectangular and triangular cross sections; from top to bottom are illustrations of tether shapes, SEM images of tether regions, and FEM (COMSOL) simulation results of the torsional mode shapes. The scale bars are $1 \mu\text{m}$. (c) Scaling of resonance frequency (left axis) and Q (right axis) with disk diameter. The curves are predictions from both analytical modeling ($f_0 = (1/2\pi)\sqrt{k_T/I}$) and FEM simulations. (d) Scaling of thermomechanical noise spectral density with disk diameter, in both voltage (left axis) and displacement (right axis) domains. The “belt”-shaped olive and purple regions (considering varying Q) show the analytical modeling for devices with rectangular and triangular tethers, respectively. The orange dashed line represents the system noise floor. In all plots, the squares and triangles show measured data (f_0 , Q , $S_v^{1/2}$, $S_x^{1/2}$) from the devices with rectangular and triangular tethers, respectively.

we plot $S_x^{1/2}$ and $S_v^{1/2}$ for all the measured devices, with analytical modeling for torsional resonators of different diameters (and therefore different resonance frequencies) with Q in the range of 150–1500, given most of the measured Q s. The responsivity \mathfrak{R} links the two vertical axes, and translates the voltage-domain noise floor $S_{v,\text{sys}}^{1/2}$ into the displacement-domain sensitivity $S_{x,\text{sys}}^{1/2}$. The scaling of thermomechanical noise spectral density is clearly presented in Fig. 3(d), with smaller devices exhibiting less thermal fluctuation.

To further understand the effect of thermal noise on the rotational motion of the devices, we calculate and plot in Fig. 4(a) the thermomechanical noise in the angular displacement domain, $S_\theta^{1/2} = \sqrt{4k_B T Q / (\omega_0 k_T)}$. Similar to $S_x^{1/2}$, we find that smaller devices (due to their higher torsional resonant frequency) has lower $S_\theta^{1/2}$. Both $S_x^{1/2}$ and $S_\theta^{1/2}$ increase with larger Q , suggesting that higher- Q devices are more responsive to external stimuli (and in the particular cases of $S_x^{1/2}$ and $S_\theta^{1/2}$, in response to the drive from the white thermal noise).

From these thermomechanical noise data one can estimate the ultimate performance of these torsional resonators when functioning as highly sensitive force and torque detectors. The force sensitivity can be calculated using $S_F^{1/2} = (\omega_0^2 M_{\text{eff}} / Q) S_x^{1/2} = \sqrt{4k_B T \omega_0 M_{\text{eff}} / Q}$ (ω_0 is the angular resonance frequency from the FEM simulation), and is plotted in Fig. 4(b). Due to the unique dependence of M_{eff} and ω_0 on the diameter, their product is almost independent of d (except when tether size and disk dimension become comparable) and therefore the force sensitivity remains roughly the same for disks with different diameters. The force sensitivities for all the measured devices are also plotted, with the best device ($d \approx 15.9 \mu\text{m}$, triangular cross-section tethers, with width $w_T \approx 1.53 \mu\text{m}$, length $L_T \approx 2 \mu\text{m}$, and thickness $t_T \approx 0.4 \mu\text{m}$) achieving $S_F^{1/2} \approx 5.7 \text{ fN}/\sqrt{\text{Hz}}$. For the rotational degree of freedom, in Fig. 4(c) we show the torque sensitivity, $S_T^{1/2} = (k_T / Q) S_\theta^{1/2} = \sqrt{4k_B T k_T / \omega_0 Q}$. Linear dependence of $S_T^{1/2}$ on d is observed. This is directly related to the independence of $S_F^{1/2}$ on device diameter, as the force arm (which relates torque to force) is proportional to the device

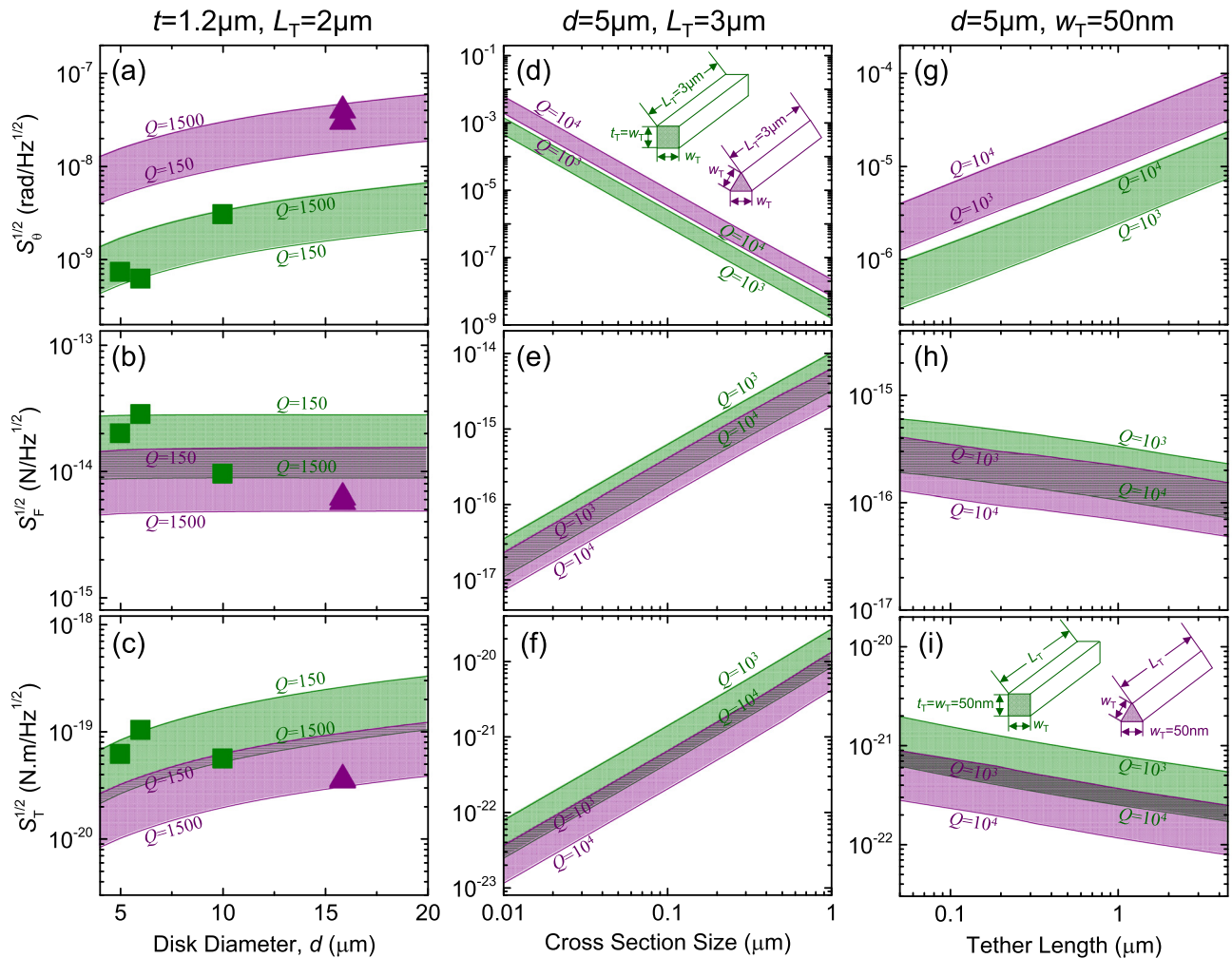


FIG. 4. Scaling of torsional resonant sensitivities with disk diameter, tether cross-sectional size, and tether length. (a)–(c) Measured angular displacement sensitivity ($S_\theta^{1/2}$), force sensitivity ($S_F^{1/2}$), and torque sensitivity ($S_T^{1/2}$) and analysis of their scaling with disk diameter. Square and triangular symbols are measured data from devices with rectangular and triangular tethers, respectively. “Belt”-like regions (considering the range of measured Q s) show the analytical predictions for these devices. (d)–(f) Sensitivities scaling with tether cross-sectional size, with a fixed tether length ($L_T = 3 \mu\text{m}$) and disk diameter ($d = 5 \mu\text{m}$). (g)–(i) Sensitivities scaling with tether length, while keeping a fixed cross-sectional width ($w_T = 50 \text{ nm}$) and disk diameter ($d = 5 \mu\text{m}$). Insets of (d) and (i) show the illustrations of the tether dimensions. In all plots, the “belt”-shaped olive and purple regions (considering varying Q) show the analytical modeling for devices with rectangular and triangular tethers, respectively. In (d)–(i), the disk thickness is kept the same as the tether thickness.

lateral dimension (d). We also plot the torque sensitivity for all the measured devices, with the best one exhibiting $S_T^{1/2} \approx 3.5 \times 10^{-20}$ (Nm)/ $\sqrt{\text{Hz}}$. In contrast to $S_F^{1/2}$ and $S_\theta^{1/2}$ which increase with Q (more fluctuation), $S_F^{1/2}$ and $S_T^{1/2}$ both decrease with higher Q , as the device becomes more responsive to external stimuli. All these four parameters increase with device size, indicating that smaller devices have higher sensitivities in all these examined measures. Devices with triangular cross-section tethers show better performance because these tethers offer smaller k_T values, especially as the tethers are thinned down in the FIB process.

We further study sensitivity scaling with the cross-sectional size and length of the tether (Figs. 4(d)–4(i)), to gain more understanding of the effects from the tethers. By varying the width (w_T) of both square and triangular cross-section tethers from 10 nm to 1 μm and computing the resonance characteristics, we estimate $S_F^{1/2} \approx 7$ aN/ $\sqrt{\text{Hz}}$, $S_T^{1/2} \approx 1 \times 10^{-23}$ (Nm)/ $\sqrt{\text{Hz}}$, and $S_\theta^{1/2} \approx 0.006$ rad/ $\sqrt{\text{Hz}}$ for devices with 10 nm-wide tethers (Figs. 4(d)–4(f)). This clearly demonstrates that thinner tethers offer smaller torsional spring constants, making the torsional mode more responsive to external stimuli. Different Q s are also considered, toward higher Q s attainable in such torsional-mode resonators. The result is consistent with scaling disk diameters, with higher Q resulting in better sensitivity. By fixing the cross-sectional dimensions of the tethers to be $w_T = t_T = 50$ nm (i.e., tethers become thin SiC nanowires, which are achievable already in practical nanofabrication³⁴), we also analyze the effects of scaling the tether length. Figures 4(g)–4(i) demonstrate quantitative results, confirming that longer tethers offer better force and torque sensitivities by reducing the torsional spring constants.

In conclusion, we have demonstrated “smart-cut” single-crystal 6H-SiC microdisk torsional resonators and studied their fundamental resonant sensitivities and scaling capabilities. By measuring intrinsic thermomechanical motion and driven resonances, and investigating devices with varying disk dimensions as well as tether shapes and sizes, we have shown how these variations affect the noise floors in detecting force, torque, and linear/angular displacement. These provide guidelines for designing high-performance resonant sensors based on the smart-cut 6H-SiC device platform. Not only harsh-environment applications established for SiC but also the combination of the wide bandgap and torsional resonators enables new opportunities such as sensing of radiation of photons with different energies.³⁵ The device and measurement techniques in this work can be readily extended to other smart-cut materials (e.g., single-crystal Si on SiO₂, 4H-SiC on SiO₂, etc.). The fundamental design guidelines and scaling laws revealed in this work are also applicable to torsional resonators in other materials.

We thank Case School of Engineering, the T. Keith Glennan Fellowship and the CSC Fellowship (No.

2011625071). We thank Dr. X. C. Zhang for helpful discussions.

- ¹A. N. Cleland and M. L. Roukes, *Nature* **392**, 160 (1998).
- ²D. Rugar, R. Budakian, H. J. Mamin, and B. W. Chiu, *Nature* **430**, 329 (2004).
- ³J. Moser, J. Güttinger, A. Eichler, M. J. Esplandiu, D. E. Liu, M. I. Dykman, and A. Bachtold, *Nat. Nanotechnol.* **8**, 493 (2013).
- ⁴R. G. Knobel and A. N. Cleland, *Nature* **424**, 291 (2003).
- ⁵M. D. LaHaye, O. Buu, B. Camarota, and K. C. Schwab, *Science* **304**, 74 (2004).
- ⁶Y. T. Yang, C. Callegari, X. L. Feng, K. L. Ekinci, and M. L. Roukes, *Nano Lett.* **6**, 583 (2006).
- ⁷J. Chaste, A. Eichler, J. Moser, G. Ceballos, R. Rurali, and A. Bachtold, *Nat. Nanotechnol.* **7**, 301 (2012).
- ⁸R. A. Johnson, *Mechanical Filters in Electronics* (John Wiley & Sons Inc., New York, 1983).
- ⁹A. N. Cleland, *Foundations of Nanomechanics* (Springer, Berlin, 2003).
- ¹⁰D. W. Carr, S. Evoy, L. Sekaric, H. G. Craighead, and J. M. Parpia, *Appl. Phys. Lett.* **77**, 1545 (2000).
- ¹¹A. Olkhovets, S. Evoy, D. W. Carr, J. M. Parpia, and H. G. Craighead, *J. Vac. Sci. Technol., B* **18**, 3549 (2000).
- ¹²P. Mohanty, D. A. Harrington, and M. L. Roukes, *Physica B* **284–288**, 2143 (2000).
- ¹³B. H. Houston, D. M. Photiadis, J. F. Vignola, M. H. Marcus, X. Liu, D. Czaplewski, L. Sekaric, J. Butler, P. Pehrsson, and J. A. Bucaro, *Mater. Sci. & Eng. A* **370**, 407 (2004).
- ¹⁴D. Antonio and H. Pastoriza, *J. Microelectromech. Syst.* **18**, 1396 (2009).
- ¹⁵X. C. Zhang, E. B. Myers, J. E. Sader, and M. L. Roukes, *Nano Lett.* **13**, 1528 (2013).
- ¹⁶J. Losby, J. A. J. Burgess, Z. Diao, D. C. Fortin, W. K. Hiebert, and M. R. Freeman, *J. Appl. Phys.* **111**, 07D305 (2012).
- ¹⁷J. P. Davis, D. Vick, D. C. Fortin, J. A. J. Burgess, W. K. Hiebert, and M. R. Freeman, *Appl. Phys. Lett.* **96**, 072513 (2010).
- ¹⁸P. H. Kim, C. Doolin, B. D. Hauer, A. J. R. MacDonald, M. R. Freeman, P. E. Barclay, and J. P. Davis, *Appl. Phys. Lett.* **102**, 053102 (2013).
- ¹⁹X. Xia, Z. Zhang, and X. Li, *J. Micromech. Microeng.* **18**, 035028 (2008).
- ²⁰O. Sahin, S. Magonov, C. Su, C. F. Quate, and O. Solgaard, *Nat. Nanotechnol.* **2**, 507 (2007).
- ²¹T. Cohen-Karni, L. Segev, O. Srur-Lavi, S. R. Cohen, and E. Joselevich, *Nat. Nanotechnol.* **1**, 36 (2006).
- ²²*Silicon Carbide*, edited by P. Friedrichs, T. Kimoto, L. Ley, and G. Pensl (Wiley-VCH, Weinheim, 2010).
- ²³*Properties of Silicon Carbide*, edited by G. L. Harris (INSPEC, London, 1995).
- ²⁴P. G. Neudeck, R. S. Okojie, and L.-Y. Chen, *Proc. IEEE* **90**, 1065 (2002).
- ²⁵M. Mehregany, C. A. Zorman, N. Rajan, and C. H. Wu, *Proc. IEEE* **86**, 1594 (1998).
- ²⁶S. Habermehl, M. Rodriguez, and B. Simmons, *J. Appl. Phys.* **112**, 013535 (2012).
- ²⁷X. M. H. Huang, X. L. Feng, M. K. Prakash, S. Kumar, C. A. Zorman, M. Mehregany, and M. L. Roukes, *Mater. Sci. Forum* **457–460**, 1531 (2004).
- ²⁸T. K. Hossain, S. MacLaren, J. M. Engel, C. Liu, I. Adesida, and R. S. Okojie, *J. Micromech. Microeng.* **16**, 751 (2006).
- ²⁹P. Cong and D. J. Young, *J. Micromech. Microeng.* **15**, 2243 (2005).
- ³⁰J. Lee, Z. Wang, K. He, J. Shan, and P. X.-L. Feng, *ACS Nano* **7**, 6086 (2013).
- ³¹W. C. Young and R. G. Budynas, *Roark's Formulas for Stress and Strain* (McGraw-Hill, New York, 2002), pp. 381–426.
- ³²J. M. Gere and B. J. Goodno, *Mechanics of Materials* (Cengage Learning, Stamford, 2013), pp. 1063–1068.
- ³³M. C. Cross and R. Lifshitz, *Phys. Rev. B* **64**, 085324 (2001).
- ³⁴X. L. Feng, M. H. Matheny, C. A. Zorman, M. Mehregany, and M. L. Roukes, *Nano Lett.* **10**, 2891 (2010).
- ³⁵R. Yang, K. Ladhane, Z. Wang, J. Lee, D. J. Young, and P. X.-L. Feng, in *Proc. IEEE 27th Int. Conf. of Micro Electro Mechanical Systems (MEMS)*, San Francisco, CA, 26–30 January 2014, pp. 793–796.